

X-ray to NIR emission from AA Tauri during the dim state

Occultation of the inner disk and gas-to-dust ratio of the absorber

P. C. Schneider^{1,2}, K. France^{3,7}, H. M. Günther⁴, G. J. Herczeg⁵, J. Robrade², J. Bouvier⁶, M. McJunkin³, and J. H. M. M. Schmitt²

¹ European Space Research and Technology Centre (ESA/ESTEC), Keplerlaan 1, 2201 AZ Noordwijk, The Netherlands e-mail: christian.schneider@esa.int

² Hamburger Sternwarte, Gojenbergsweg 112, Hamburg, 21029 Germany

³ Center for Astrophysics and Space Astronomy, University of Colorado, 389 UCB, Boulder, CO 80309, USA

⁴ Harvard-Smithsonian Center for Astrophysics, 60 Garden Street, Cambridge, MA 02139, USA

⁵ The Kavli Institute for Astronomy and Astrophysics, Peking University, Yi He Yuan Lu 5, Hai Dian Qu, Beijing 100871, China

⁶ Univ. Grenoble Alpes, IPAG, F-38000 Grenoble, France

CNRS, IPAG, F-38000 Grenoble, France

⁷ Laboratory for Atmospheric and Space Physics, University of Colorado, 392 UCB, Boulder, CO 80309

Received 24/12/2014; accepted 20/08/2015.

ABSTRACT

AA Tau is a well-studied, nearby classical T Tauri star, which is viewed almost edge-on. A warp in its inner disk periodically eclipses the central star, causing a clear modulation of its optical light curve. The system underwent a major dimming event beginning in 2011 caused by an extra absorber, which is most likely associated with additional disk material in the line of sight toward the central source. We present new XMM-Newton X-ray, Hubble Space Telescope FUV, and ground based optical and near-infrared data of the system obtained in 2013 during the long-lasting dim phase. The line width decrease of the fluorescent H₂ disk emission shows that the extra absorber is located at $r > 1$ au. Comparison of X-ray absorption (N_H) with dust extinction (A_V), as derived from measurements obtained one inner disk orbit (eight days) after the X-ray measurement, indicates that the gas-to-dust ratio as probed by the N_H to A_V ratio of the extra absorber is compatible with the ISM ratio. Combining both results suggests that the extra absorber, i.e., material at $r > 1$ au, has no significant gas excess in contrast to the elevated gas-to-dust ratio previously derived for material in the inner region ($\lesssim 0.1$ au).

Key words. Stars: individual: AA Tau, Stars: low-mass, stars: pre-main sequence, stars: variables: T Tauri, Herbig Ae/Be, X-rays: stars, Ultraviolet: stars

1. Introduction

Disks around protostars play a key role in star formation and influence many features of the final stellar system. For example, most of the stellar mass is acquired by disk accretion, the rotation period is set by magnetic interaction with the disk, and planets form within the disk. These so-called accretion or protoplanetary disks contain approximately 10^{-3} to $10^{-1} M_\odot$ and disperse within a typical time span of a few Myrs (see review by Alexander et al. 2014), which also sets the time scale for planet formation. Within this time, disks undergo large structural changes. In particular, grains grow to larger sizes, and larger grains are thought to settle in the disk midplane leaving a gas rich disk atmosphere behind (see review by Williams & Cieza 2011).

Gas comprises the majority of the mass in a protoplanetary disk, with only a small fraction contributed by dust. The canonical gas-to-dust ratio of 100:1 found in the interstellar medium is often also assumed for protoplanetary disks. Therefore, the gas content controls essential transport processes within the disk like angular momentum redistribution and dust grain motion. Gas affects grain growth through the coupling of gas and dust dynamics (Weidenschilling 1977; Takeuchi & Artymowicz 2001), as well as the thermal and chemical balance of the disk (e.g., Woitke et al. 2009).

Measuring the disk's dust content is relatively straightforward because the thermal dust emission is readily observable at infrared and radio wavelengths. However, measuring the gas content of protoplanetary disks is more challenging. Observational studies often rely on gas emission lines, but their interpretation is highly model dependent. For example, Tilling et al. (2012) modeled the disk around the Herbig Ae star HD 163296 and found gas-to-dust ratios between 9:1 and 100:1 depending on their model assumptions. A specific problem is that the bright CO emission can become optically thick, so that only part of the gas mass is traced (e.g., Hughes et al. 2008) and that CO freezes-out on grains at low (~ 20 K) temperatures in the disk midplane. In addition, gas and dust emission are not necessarily co-spatial, thus introducing additional uncertainties into the local gas-to-dust ratio.

Transmission spectroscopy is a different approach to studying the gas content of (nearly) edge-on disks (e.g., Lahuis et al. 2006; Rettig et al. 2006; Schneider & Schmitt 2010; Horne et al. 2012; France et al. 2012a; McJunkin et al. 2013). In particular, X-ray absorption provides a complementary view of the gas-to-dust ratio, because it is sensitive to the total amount of material in the line of sight, i.e., it is largely dominated by gas in most scenarios. Comparing X-ray and dust extinction thus provides

an estimate of the gas-to-dust ratio for a given line of sight. This estimate depends on different assumptions than gas emission line studies, e.g., the total X-ray absorption is dominated by He and heavier elements (e.g., oxygen, carbon, iron) and not by hydrogen, which represents the main component of protoplanetary disks. Therefore, transforming the X-ray absorption to an equivalent hydrogen column density implicitly assumes a particular abundance pattern.

Here, we use X-ray absorption spectroscopy to study the disk around the classical T Tauri star (CTTS) AA Tau. A so far unique dimming event of the system allows us to study new regions of the disk using transmission spectroscopy. Combined with new measurements of the dust extinction from optical and near-IR (NIR) photometry and new Hubble Space Telescope (HST) far-ultraviolet (FUV) spectroscopy of disk emission lines, we derive the disk’s gas-to-dust ratio and provide an estimate for the disk region traced by this measurement.

Our paper is structured as follows. We start with a brief description of the AA Tau system in the next section (sect. 2) and describe observations and data analysis in sect. 3. Using the X-ray data, we measure essentially the gas column toward the stellar source in sect. 4. Using optical and near-IR data, we derive the dust content of the line of sight in sect. 5. We then compare the dust extinction with the absorbing gas column derived from the X-ray data to study the gas-to-dust ratio (sect. 6). In sect. 7 we study fluorescent H_2 line emission from the disk surface to constrain the location of the extra absorber. We close with a summary and discussion in sect. 8.

2. AA Tau: An almost edge-on CTTS

AA Tau is a well-studied low-mass CTTS in the Taurus star forming region at a distance of 140 pc (Kenyon et al. 1994). Its spectral type is M0.6 – K7 with an A_V of 0.4 – 0.8 (Herczeg & Hillenbrand 2014; Bouvier et al. 1999, resp.). We adapt $M_\star \approx 0.8 M_\odot$ as estimated by Bouvier et al. (1999). Disk accretion rates between 10^{-9} and $10^{-8} M_\odot \text{ yr}^{-1}$ have been derived (e.g., Basri & Bertout 1989; Valenti et al. 1993; Gullbring et al. 1998; Bouvier et al. 2003, 2013). The AA Tau system is seen close to edge-on ($i \sim 75^\circ$) so that the light passes through the upper layers of its protoplanetary disk (e.g., Bouvier et al. 2003; Cox et al. 2013).

AA Tau is the prototype of stars showing periodic features in their optical light curves caused by variable line of sight extinction. These so-called AA Tau-like variables show a stable maximum brightness and pronounced, periodic minima (with $\Delta V \approx 1 - 2$ mag). These minima are most likely caused by a disk warp that periodically (partially) occults the star. For AA Tau, the typical eclipse depth during the last 24 years is approximately 1.0 to 1.6 mag while there are also short periods in time when no or only little additional extinction is seen (Bouvier et al. 2003). Assuming Keplerian rotation, the observed periodicity of about eight days indicates that the warp is located at 0.07 au, i.e., very close to the inner edge of the dust disk. We refer to this feature as the “inner warp” in the following.

The periodicity of the extinction allows one to separate the features of the inner warp from those of other absorbers along the line of sight. Bouvier et al. (2007) suggest that the grains in the inner warp are larger than in the ISM. Schmitt & Robrade (2007) show from their analysis of a series of XMM-Newton observations that the line of sight passes through material with a gas-to-dust ratio about ten times higher than in the ISM and associate this gas excess with a dust-depleted outflow or dust-

free accretion streams (see also Grosso et al. 2007, for a detailed analysis of these X-ray data in the multi-wavelengths context).

The gas content along the line of sight was also studied using high-resolution FUV observations. HST COS observations have shown that the neutral atomic hydrogen column density toward AA Tau is $4 - 5 \times 10^{20} \text{ cm}^{-2}$ (France et al. 2012a; McJunkin et al. 2014). This is lower than the minimum expected from the optical extinction ($A_V = 0.4 - 0.8$) for an ISM-like gas-to-dust ratio and at least a factor of 18 below the column density derived from X-ray observations. This discrepancy is probably caused by a high molecular fraction within the circumstellar material, leaving little atomic hydrogen in the disk atmosphere, as shown by France et al. (2014a) for RW Aur (a CTTS in a comparable evolutionary stage as AA Tau). Molecular absorption lines have also been measured in the FUV with H_2 absorption tracing the hot ($T \sim 2500$ K) molecular content ($N_{H_2} = 8^{+22}_{-4} \times 10^{17} \text{ cm}^{-2}$, see France et al. 2012a) and CO absorption bands tracing the warm ($T \sim 500$ K) molecular material ($N_{CO} = 3^{+7}_{-2} \times 10^{17} \text{ cm}^{-2}$, see France et al. 2012a; McJunkin et al. 2013). For the canonical H_2 to CO ratio ($\sim 10^4$, e.g., Lacy et al. 1994) one would therefore expect an absorbing column density of $\gtrsim 10^{22} \text{ cm}^{-2}$ in agreement with the X-ray data ($N_H \sim 1 - 2 \times 10^{22} \text{ cm}^{-2}$).

Recently, Bouvier et al. (2013) have reported that AA Tau experienced an unexpected drop in its optical brightness by about 2 mag in the V band toward the end of 2011. Figure 1 shows the optical light curve with the dates of the analyzed observations marked. In the following, we denote the new state as the “dim state” and the previous state at higher optical luminosity as the “bright state”. The most likely explanation for the dimming is that a part of the disk located farther out than the inner warp is eclipsing the system, because emission from the star is obscured, but the spatially extended jet emission has not changed. We term the origin of the increased extinction the “extra absorber” in the following. From time-scale arguments, Bouvier et al. (2013) estimated a radius of about eight au for the obscuring material and their VLT-Xshooter observations during the dim state show no change in mass accretion rate onto AA Tau. The wavelength dependence of the additional reddening suggests that scattered light contributes a large fraction of the blue-optical flux during the dim state contrary to the bright state for which Bouvier et al. (1999) estimated a negligible scattering fraction. Thus, scattering of optical photons likely contributes also to our new 2013 data.

3. Observations and data analysis

Table 1 lists the new X-ray, FUV, optical and NIR data obtained during the dim state of AA Tau. Specifically, we obtained new XMM-Newton data to measure the gas content of the line of sight (sect. 3.1) and new (near-) simultaneous optical (NIR) data that trace the dust content (sect. 3.2). In addition, we use new HST COS data described in sect. 3.3 to study H_2 emission lines originating in the disk surface to constrain the location of the extra absorber.

3.1. XMM-Newton X-ray data

The new XMM-Newton observations of AA Tau during the dim state were performed on 2013 August 15 for 34 ks. We concentrate on the EPIC CCD spectra obtained with MOS1, MOS2, and pn (for instrument descriptions see Turner et al. 2001; Strüder et al. 2001). XMM-Newton data reduction has been performed

Table 1. Analyzed observations

Observing date	Observatory	Instrument	Filter/grating	Exp. time	Approx. wavelengths	Obs. ID.
2013 Aug 15	XMM-Newton	EPIC	Medium	34 ks	3 – 30 Å	0727960501
		OM	V, B UVW1, UVW2	6.0 ks each 6.5, 6.7 ks	551, 445 nm ≈300, 212 nm	
2011 Jan 06	HST	COS	G160M G130M	4.2 ks 5.7 ks	1133 – 1795 Å	11616
2013 Feb 06 2013 Feb 05	HST	COS	G160M G130M	8.7 ks 18.2 ks	1065 – 1790 Å ^a	12876
2013 Aug 23	UKIRT	WFCAM	J, H, K	5 × 1 s	1.25, 1.65, 2.2 μm	U/13A/H28B
2013 Oct 16 2013 Oct 17 2013 Oct 21	CAHA	Omega 2000	J, H, K	4 × 8 s	1.25, 1.65, 2.2 μm	DDT

^a With ~10 Å and 25 Å gaps around 1217 and 1375 Å, respectively

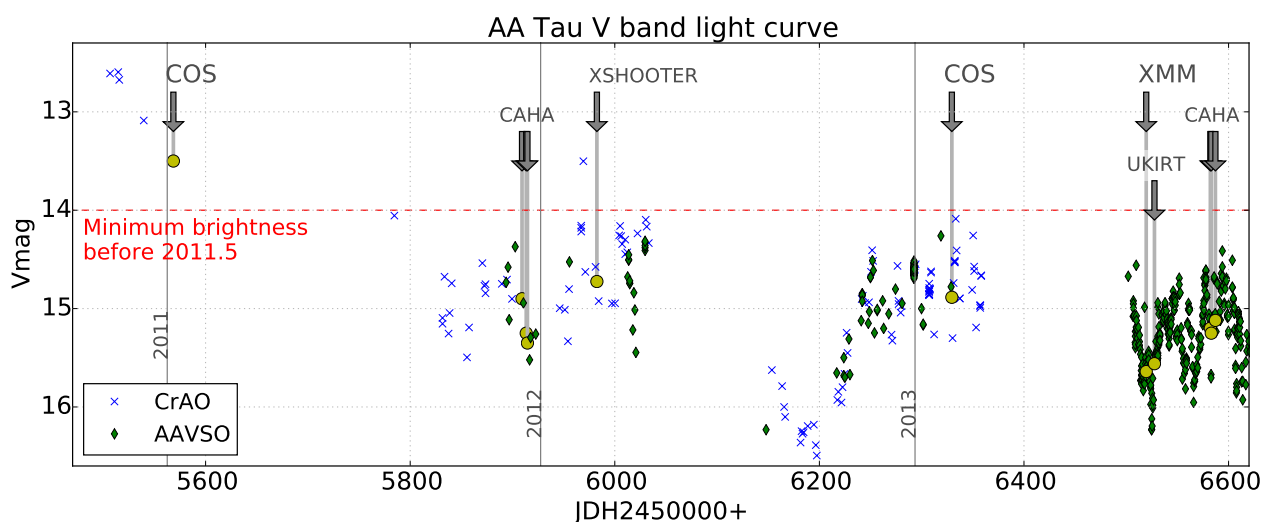


Fig. 1. V-band light curve of AA Tau in heliocentric Julian date. The important observations are labeled. The yellow circles indicate the estimated brightness during these observations. The red, dashed line indicates the lowest state prior to the dimming.

using SAS version 12¹. Periods of enhanced particle background have been excluded from the spectral analysis. Filtered exposure times are 28.6 ks for pn and 33.3 ks for each MOS detector. There are no strong flares in the X-ray light curve and we fit the entire observation with a single set of parameters. The three EPIC spectra were fitted simultaneously using XSPEC (Arnaud 1996). Therefore, the fits are dominated by the pn data as the pn detector provides the highest count number. We used an absorbed APEC model (Smith et al. 2001) for the spectral modeling (XSPEC notation: `phabs * vapec`) as in Schmitt & Robrade (2007) and adopt their plasma abundances for consistency. The `phabs` model uses the absorption cross sections of Balucinska-Church & McCammon (1992) and we used elemental abundances for the absorber according to Anders & Grevesse (1989). The equivalent hydrogen column density (N_H) depends on the abundances assumed for the absorber; a lower metallicity implies a higher N_H . Unless noted otherwise, we use the Anders & Grevesse (1989) abundances for the absorber to be consistent with previous X-ray studies of AA Tau. For the relevant photon energy range ($E_{phot} > 1.0$ keV) differences between this absorp-

tion model and the `wabs` model used by Grosso et al. (2007) are negligible. Errors indicating 90 % confidence ranges are provided for the X-ray data.

To compare the dim state with the previous bright state, we use archival XMM-Newton data from an observing campaign that obtained eight snapshots in 2003 covering two rotation periods of the inner disk warp; these data have previously been published by Schmitt & Robrade (2007) and Grosso et al. (2007).

3.2. Optical and near-IR data around the XMM-Newton observation

The evolution of the optical and NIR magnitudes of AA Tau depends on the dust content of the line of sight and we use new optical/NIR data to estimate the dust extinction during the XMM-Newton observation.

During the X-ray observation, we obtained simultaneous V, B, UVW1, and UVW2 images with the optical monitor (OM) on-board of XMM-Newton. The pipeline source detection reports magnitudes of 15.63 ± 0.01 , 17.16 ± 0.02 , and 17.38 ± 0.08 for the V, B, and UVW1 filters using the data from Exp.IDs

¹ <http://xmm.esac.esa.int/sas/>

Table 2. Near-IR magnitudes of AA Tau.

Date	Observ.	V^1	J	H	K	Ref.
1995 Nov 16 ²	CAMILA	13.9	9.99	9.14	8.55	(1)
1995 Nov 21 ³	CAMILA	12.6	9.30	8.6	8.11	(1)
1997 Nov 30	2MASS	–	9.43	8.55	8.05 ⁴	(2)
2011 Dec 13		14.9	10.46	9.20	8.46	
2011 Dec 17	CAHA	15.3	10.61	9.27	8.43	(3)
2011 Dec 19		15.4	10.53	9.21	8.45	
2013 Aug 23	UKIRT	15.54	11.13	10.13	9.70	(4)
2013 Oct 16		15.17	11.00	9.63	8.81	
2013 Oct 17	CAHA	15.15	10.85	9.52	8.65	(4)
2013 Oct 21		15.05	10.59	9.32	8.58	

Notes. ⁽¹⁾ Estimated from the data points close in time to the NIR measurements. ⁽²⁾ Inner warp in front of AA Tau. ⁽³⁾ Inner warp behind AA Tau. ⁽⁴⁾ The 2MASS filter is K_s and not K.

References. (1) Bouvier et al. (1999); (2) Skrutskie et al. (2006); (3) Bouvier et al. (2013); (4) This work

S006 – S008. The UVW1 filter is centered on the bright Mg II doublet that is known to be jet related, i.e., we do not consider it as a good tracer of photometric emission, but include it in Fig. 5 for completeness. The B and V magnitudes are within the range of previous measurements during the dim state (Bouvier et al. 2013) so that the V magnitude is 1.6 to 3.1 mag below the values during the 2003 XMM-Newton observing campaign. No source is found by the detection algorithm in the UVW2 exposure, but extracting the counts in a circle with a radius of 4.8 arcsec (10 pixel) the UVW2 exposure ($\lambda_{cen} = 2120 \text{ \AA}$) shows slight excess counts above the expected background at the position of AA Tau significant at about 90% confidence level². The approximate magnitude is $19.4^{+2.2}_{-0.4}$. Compared to the 2003 XMM-Newton campaign when the OM was also operated with the UVW2 filter, this is nominally 2.6 – 3.6 mag darker (observed magnitude range in 2003: ~ 15.8 – 16.8 mag).

In addition, AA Tau has been monitored around the XMM-Newton observation by the Crimean Astrophysical Observatory (CrAO, K. Grankin, priv. communication) and by astronomers around the world organized through the AAVSO (Henden, A.A., 2013, Observations from the AAVSO International Database, <http://www.aavso.org>). These data provide the frame to study periodic features in the light curve as expected from the inner warp.

Near-IR data were obtained by UKIRT³ and by Omega2000⁴ at the Calar-Alto 3.5 m telescope (CAHA). Pipeline reduction has been used for the UKIRT data and custom python routines for the Omega2000 data including sky subtraction and flat-fielding. Table 2 lists the resulting near-IR magnitudes of AA Tau together with estimates of the V magnitude during the near-IR observations from nearby optical data points. This gives a J magnitude around 11 at V=15.6. The corresponding H and K band magnitudes are about 10 and 9.7, respectively.

For the XMM-Newton observation, we estimate the near-IR magnitudes from the nearest measurements as no simultaneous observations exist, i.e., from the UKIRT data that were obtained at approximately similar optical brightness. Fortunately, the UKIRT data have been obtained about eight days after the

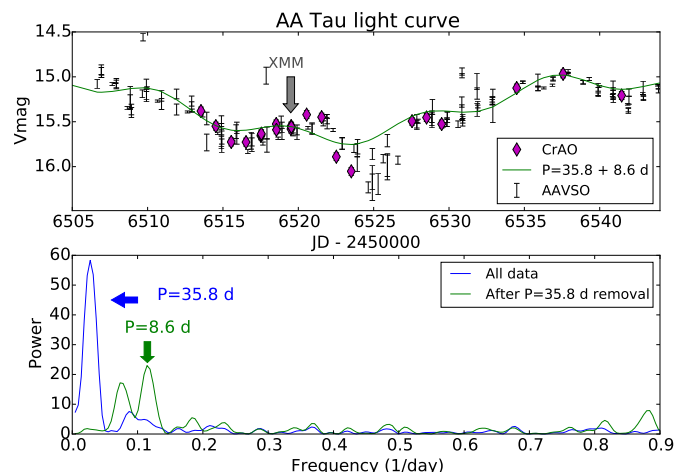


Fig. 2. Top: Close-up of the optical light curve around the XMM-Newton observation with sinusoidal models. **Bottom:** Lomb-Scargle diagram with the peaks marked.

XMM-Newton observation so that both observations trace the same phase with respect to the inner disk warp.

Figure 2 (top) shows a close-up of the optical light curve around the XMM-Newton observation. AA Tau showed periodic variations in its light curve in the bright state and we search for similar variability in the new optical data (starting MJD 2456501) using Lomb-Scargle periodograms (Fig. 2 bottom, phased light curves are provided in Fig. B.1). The light curve shows variation on a time scale much longer than the original eight day period as indicated by the 36 day peak in the periodogram. We remove this long term trend from the light curve and find a modulation with an 8.6 day period, which is very close to the original 8.19 day periodicity (Artemenko et al. 2012, statistical false alarm probability is 10^{-9}). The good match between both periods shows that variability caused by the inner warp is still present in the optical light curve. The derived period is probably influenced by a longer, possibly irregular pattern. We think that a comparable additional modulation of the light curve might be responsible for the fact that the optical data presented by Bouvier et al. (2013) did not show a significant periodicity if analyzed as one single data set, but that a significant periodic signal was found in a specific three month time interval with an amplitude of 0.7 mag in the V band. In fact, the modulation amplitude is expected to vary as the ratio between direct and scattered light changes with absolute magnitude. Inspection of Fig. 2 reveals that the XMM-Newton observation was obtained when the majority of the inner warp was not in the line of sight towards AA Tau. The statistical uncertainty of the phase is small, so that we think that a reasonable estimate of the phase uncertainty is rather given by the phase difference that results from leaving the period as a free fit parameter ($P = 8.6$ day model) and a model with the period set to its previous value ($P = 8.19$ days), i.e., we consider a phase uncertainty of 0.2 or 1.6 days as a reasonable estimate.

3.3. FUV spectra from HST COS

Two HST COS FUV observations of AA Tau exist. The 2011 data, published by France et al. (2012a), were obtained during the bright state while the 2013 FUV data were obtained during the dim state. Thus, changes in the disk emission between both epochs allow us to put constraints on the location of the extra absorber.

² The statistical error is given by the chance to find the number of detected source photons by a random background fluctuation.

³ See www.ukirt.hawaii.edu

⁴ www.caha.es/CAHA/Instruments/O2000/index.html

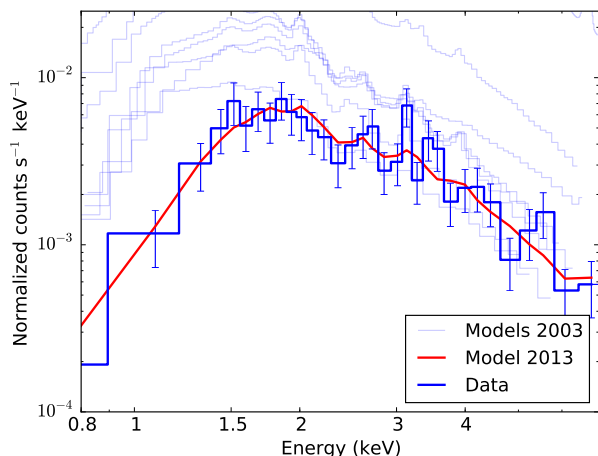


Fig. 3. Comparison of the X-ray spectrum during the dim state with models for the archival X-ray spectra obtained during the bright state (Models 2003). The pn-spectrum binned to 15 counts per bin is shown as Data.

The wavelength ranges covered by the COS observations are listed in Tab. 1 and multiple FP offsets have been used to mitigate the effects of fixed pattern noise. The COS FUV data of both epochs were processed as described in detail by France et al. (2014b). The one-dimensional spectra produced by the COS calibration pipeline, CALCOS, were aligned and co-added using custom software procedures described by Danforth et al. (2010). The analysis of the H_2 lines follows the method described in France et al. (2012b). Line profiles were obtained by weighting the individual central wavelength settings with their respective exposure time for all line fitting applications. A new observing mode (cenwave= λ 1222) was used for the short wavelength observations in 2013 to extend the available spectrum down to 1065 Å which, however, causes the loss of any information on the Ly α emission line so that changes in the atomic and molecular hydrogen absorption between both epochs must remain unexplored.

Part of the description of the FUV data can be found in the appendix. While these spectra are interesting in their own right, they are compatible with the results of the main text and do not provide additional constraints. In particular, these results relate to the evolution of the atomic emission lines, the CO emission lines, as well as the CO absorption seen against the continuum. We refer the interested reader to the respective appendix sections (App. C to F).

4. X-ray absorbing column density towards AA Tau: The line of sight's gas content

X-ray absorption is sensitive to the gas content of the line of sight and, thus, provides complementary information about the extra absorber compared to optical/NIR data which are essentially sensitive to the dust content. We derive the X-ray absorption parameterized by N_H from our new XMM-Newton data through modeling the coronal emission of AA Tau with one absorbed thermal emission component. Table 3 lists the fit results. The coronal properties (temperature and emission measure) of AA Tau derived from the new 2013 data are within the range of values observed during the 2003 XMM-Newton campaign. This indicates that the stellar source remains rather unaffected by the process(es) that changed the extinction. Figure 3 compares the new X-ray observation with models for the

Table 3. X-ray results. Fluxes are provided for the 0.2 – 10.0 keV energy range. Values for the 2003 data are taken from Schmitt & Robrade (2007). Values in brackets pertain to the 2003 observation with strongly enhanced X-ray emission. This observation stands out from the rest of the observations and might not be representative of the X-ray emission of AA Tau.

Parameter	2013	2003	Unit
Count rate ⁽¹⁾	21.6	19 – 147 (800)	counts ks ⁻¹
N_H	1.9 ± 0.3	$0.9_{+0.5}^{-0.4} - 1.7_{-0.3}^{+0.3}$	10^{22} cm ⁻²
kT	$3.1_{-0.7}^{+1.1}$	$1.8_{-0.4}^{+0.8} - 3.9_{-0.5}^{+0.7}$	keV
EM	$4.0_{-0.8}^{+1.0}$	$3.5_{-1.1}^{+1.5} - 21.6_{-2.0}^{+2.6}$ ($141.4_{-5.3}^{+5.4}$)	10^{52} cm ⁻³
$L_{X\text{ obs.}}$	2.2	1.5 – 16.4 (96.4)	10^{29} erg s ⁻¹
$L_{X\text{ emitted}}$	5.6	4.0 – 31.8 (208)	10^{29} erg s ⁻¹
$\chi^2/\text{d. o. f.}$	33.1 / 51	23/21 - 139/134 (835/801)	–

Notes. ⁽¹⁾ Summed EPIC count rate

archival XMM-Newton observations from 2003. The column density best fitting the 2013 X-ray data ($N_H = 1.9 \times 10^{22}$ cm⁻²) is slightly higher than the highest value during the 2003 observing campaign when the X-ray absorption varied between 0.9 and 1.7×10^{22} cm⁻². Assuming the Asplund et al. (2009) abundances for the absorbing material, the equivalent hydrogen column density is $N_H = 2.85_{-0.45}^{+0.47} \times 10^{22}$ cm⁻².

Although scattering must be considered for optical photons, X-ray scattering is regularly ignored in the context of CTTSs. Nevertheless, we verified that scattering is unlikely to affect the X-ray spectrum of AA Tau. At X-ray energies Thomson scattering (energy independent and only moderately angle dependent) and Rayleigh Gans scattering (energy dependence E_{phot}^{-2} and forward scattering) can contribute for gas and grain scattering, respectively. For our estimate, we assume that the scattering screen extends π sr (a quarter of the sky; a very conservative estimate) and $A_V = 5$ (for dust scattering) or $N_H = 2 \times 10^{22}$ cm⁻² (for Thomson scattering). Further assuming no absorption along the scattering light path, the maximum scattering fraction is $\lesssim 10\%$ at 1 keV (about the softest energies in the observed X-ray spectrum). Therefore, we ignore scattering when interpreting the observed X-ray spectrum of AA Tau (see also Bally et al. 2003, for a discussion of X-ray scattering in the context of CTTSs).

To estimate the absorption caused by the extra absorber, we compare the new N_H measurement with the values observed in 2003. Using the full range of the 2003 N_H values, i.e., assuming no dependence of N_H with inner disk phase (as described by Grosso et al. 2007), we find $N_H^{\text{extra}} = 0.2 \dots 1.0 \times 10^{22}$ cm⁻² with statistical errors of $0.4 - 0.5 \times 10^{22}$ cm⁻². Excluding the 2003 values closest to mid eclipse that have the highest column density ($N_H = 1.70$ and 1.73×10^{22} cm⁻²), the range reduces to $N_H^{\text{extra}} = 0.5 \dots 1.0 \times 10^{22}$ cm⁻² with similar uncertainties. Thus, the extra column density that can be associated with the extra absorber is below 1.5×10^{22} cm⁻².

5. Dust extinction towards the stellar source

We now analyze the dust extinction caused by the extra absorber during the XMM-Newton observation for comparison with the

X-ray derived column density. We denote this extra absorption with ΔA_V in the following.

Circumstellar material around CTTSs might contain processed dust so that the extinction law potentially deviates from its standard ISM form (e.g., see review by Testi et al. 2014). In addition, stellar photons might be scattered within the circumstellar environment erroneously suggesting a low dust extinction, i.e., $\Delta V \neq \Delta A_V$. Scattering is strongly wavelength dependent ($\sim \lambda^{-4}$). Therefore, we use the evolution of the NIR magnitudes to estimate the dust extinction during the X-ray observation. Specifically, we deredden the NIR colors to the CTTS locus using the Rieke & Lebofsky (1985) extinction law (see Fig. 4 bottom). This gives $A_V \approx 3.5$ for the UKIRT observation and $A_V \approx 4.5$ for the CAHA data, i.e., within 0.5 mag of the results by Bouvier et al. (2013) who estimated $A_V \approx 4$. For the bright state, most of the data points are distributed around the CTTS locus implying little to no NIR extinction (especially when considering that we are interested in the values for the situation when the inner warp is behind AA Tau). Thus, the extra absorber is responsible for most of the extinction implying $\Delta A_V \approx 4 \pm 0.5$ during the X-ray observation. As a check, we use prior knowledge on the J magnitudes of AA Tau during the bright state and attribute the drop in J magnitude to the extra absorber, i.e., we assume $\Delta J = A_J$ and transfer A_J to A_V using the Rieke & Lebofsky (1985) extinction law. We do not consider the H and K magnitudes, because they are likely affected by disk emission as suggested by the NIR color-color diagram (Fig. 4) and by the magnitude spread, which is smallest in J. Comparing the bright state with the inner warp behind AA Tau to the J magnitudes from 2013 (Tab. 2), we find $\Delta J = 1.3 - 1.8$ mag, which transforms to $A_V = 4.6 - 6.4$. This is slightly higher than the first method. The highest value ($A_V = 6.4$) pertains to the UKIRT data for which dereddening to the CTTS locus gives $A_V \approx 3.5$. Therefore, we extend the confidence range on A_V to higher values and adapt $A_V = 4.0^{+1.0}_{-0.5}$ for the dust extinction during the dim state.

Figure 5 shows the range of fluxes observed during the bright state and around the 2013 XMM-Newton observation. The broad wavelength coverage of our observations allows us to investigate if scattering contributes to the observed flux (scenario I) or if a deviation from the ISM extinction law parameterized by changing R_V can explain the observed flux evolution without scattering (scenario II). This R_V parameterization might not be entirely correct for the circumstellar environment of CTTSs, but nevertheless gives an impression of the effect and is used for illustrative purposes here. Specifically, we consider the extinction laws of Fitzpatrick (1999) and Cardelli et al. (1989) setting R_V to higher values than the canonical 3.1 to mimic grain growth in an approximate way. We do not draw conclusions based on the numerical value of R_V since we are only interested in the impact of a different grain size distribution on the extinction curve and in particular on the NIR extinction.

Dust extinction increases towards shorter wavelengths so that FUV data can provide strong constraints on the extinction. However, intrinsic variability as well as an outflow contribution hamper direct interpretation of the AA Tau data. App. D describes that the observed evolution is compatible with the two following scenarios providing no additional discriminating power.

5.1. Scenario I: Scattering

Bouvier et al. (2013) suggest that scattering causes the stellar V magnitude to decrease less strongly than expected from their

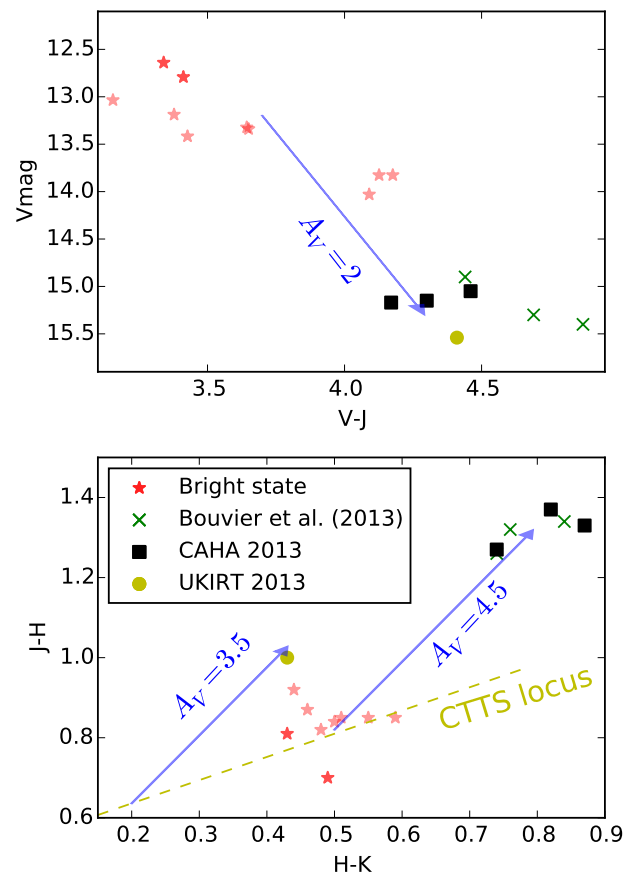


Fig. 4. Color-magnitude (top) and color-color diagrams (bottom) of AA Tau. The CTTSs locus is from Meyer et al. (1997). Extinction vectors from Rieke & Lebofsky (1985). The darker red stars for the bright state indicate measurements with the inner warp behind AA Tau.

near-IR photometry. With $\Delta A_V \sim 4$ from the NIR magnitudes and $\Delta V = 2.5$, we find a similar behavior. In this scenario, the majority of the observed optical photons do not travel through the inner warp but are scattered. This causes the amplitude of the eight day light curve modulation to decrease. A scattering fraction of a few percent causes a constant flux of $V \sim 15.6$. The remaining modulation is caused by the direct light passing through the inner warp. Assuming $\Delta A_V \approx 4.5$ suggested by the CAHA data, the optical brightness variation decreases from the value observed during the bright state ($\Delta V \approx 1.5$) to $\Delta V \approx 0.2$, i.e., reasonably close to the observed value of 0.15.

5.2. Scenario II: Dust evolution

Figure 5 shows that the Cardelli et al. (1989) extinction law with $\Delta A_V = 3.0$ and $R_V = 8.0$ approximately reproduces the observed flux evolution between the bright and dim states. Reddening the bright state fluxes matches the optical data points and the resulting near-IR magnitudes are close to the brightest values observed during the dim state. However, the magnitudes observed around the 2013 XMM-Newton observation are rather high compared to the full range of observed magnitudes (see sect. 3.2). Using even higher R_V values cannot bring these NIR magnitudes in agreement with the optical/NUV magnitudes. This tension might be caused by time variability between the XMM-Newton and NIR observations. However, the observed decrease of the eight

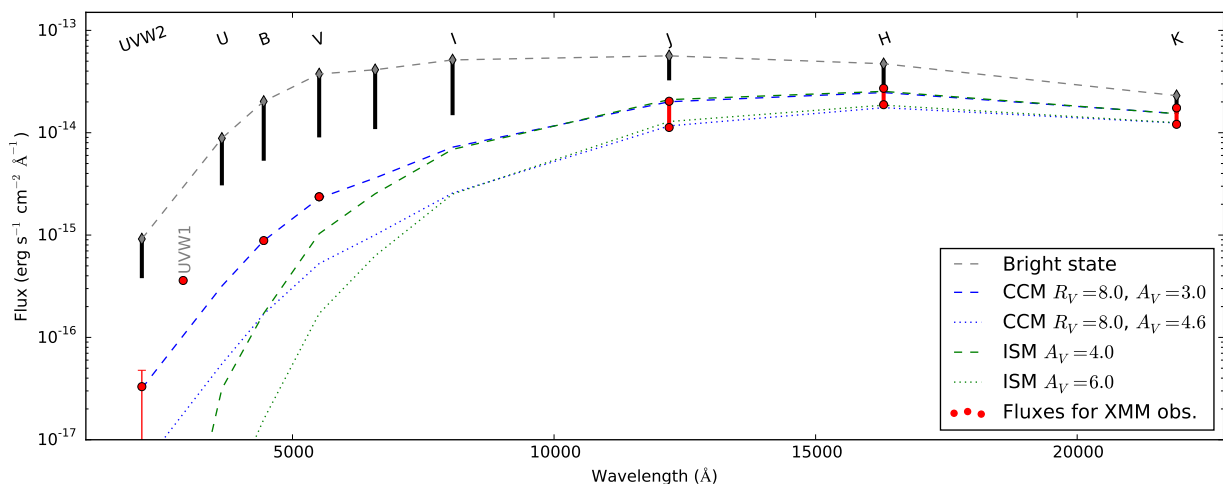


Fig. 5. Fluxes for the AA Tau system during the bright and dim state. During the bright state the observed photospheric emission was modulated by the inner warp and the gray bars indicate the ranges for each filter. The fluxes during the XMM-Newton observation are shown as red circles. The red bars indicate the range of NIR magnitudes observed during the dim state. The gray, dashed line indicates the unclipped SED during the bright state for comparison with the dim state during the XMM-Newton observation. Finally, the blue and green lines (dashed and dotted) show the expected flux distribution taking the gray line as the reference assuming different extinction laws (CCM refers to the Cardelli et al. 1989, extinction law).

day optical light modulation due to the inner warp is not expected within this scenario and would require changes within the AA Tau system in addition to an extra absorber. Applying the Fitzpatrick (1999) extinction law results in steeper (redder) spectral energy distributions than the Cardelli et al. (1989) models and fits the data less well.

In summary, the scattering scenario is compatible with the available data while the grain growth scenario requires additional model modifications to reconcile the data. Therefore, we consider scattering more likely. Its strong wavelengths dependence allows us to estimate $\Delta A_V = 4.0^{+1.0}_{-0.5}$ during the XMM-Newton observation in 2013.

6. Comparing N_H and A_V

Using the gas absorption characterized by N_H , measured from the X-ray data, and the dust extinction from the optical/NIR data described by A_V , we evaluate the gas-to-dust ratio of the extra absorber and compare it to previous measurements during the bright state. We use $A_V \approx 4.0^{+1.0}_{-0.5}$ for the dust extinction caused by the extra absorber (see sect. 5) and the full range gas column densities found in sect. 4 ($N_H^{\text{extra}} = 0.2 \dots 1.0 \pm 0.5 \times 10^{22} \text{ cm}^{-2}$). This results in $N_H = 0.5 \dots 2.5 \pm 1.4 \times 10^{21} \text{ cm}^{-2} A_V^{-1}$, which is compatible with the ISM value of $N_H = 1.8 \times 10^{21} \text{ cm}^{-2} A_V^{-1}$ (e.g., Predehl & Schmitt 1995). This ratio is lower than the about ten times elevated gas content found during the 2003 XMM-Newton campaign and suggests that the extra absorber is less gas-rich than the material in the line of sight of the 2003 observations.

Within the uncertainty margin a gas free absorber as well as a slightly gas-rich composition are possible. Within about 0.1 au, one finds that N_H/A_V is of the order of $10^{22} \text{ cm}^{-2} A_V^{-1}$ (see sect. 2), i.e., about an order of magnitude above the ratio for the extra absorber. This shows that the extra absorption is not caused by material with the same gas-to-dust ratio as found in the inner region of the AA Tau system.

7. H_2 disk emission: The location of the extra absorber

Bouvier et al. (2013) suggest that the extra absorber is located several au from AA Tau. This is compatible with the optical light curve showing less pronounced modulation as well as with the lower N_H/A_V value, which suggests that the extra absorber's composition is different from the material within 0.1 au. Here, we use the evolution of the molecular hydrogen emission thought to originate in the upper disk layers to put further constraints on the location of the extra absorber.

H_2 at temperatures around $2 - 3 \times 10^3 \text{ K}$ is fluorescently pumped by stellar $\text{Ly}\alpha$ photons and decays primarily via discrete transitions in the FUV. The spatial origin of the H_2 emission lines is imprinted in their observed velocity structure since the dominant broadening mechanism of these lines is the Doppler shift due to Keplerian rotation around the central star (France et al. 2012b). Therefore, comparing the velocity structure of the H_2 emission during the dim and the bright state constrains the disk location obscured by the extra absorber.

7.1. Evolution of the line profile

Figure 6 shows the evolution of the three strongest H_2 progressions and Tab. G.1 lists the general properties of the securely detected fluorescence routes. All detected H_2 emission lines are associated with progressions pumped by $\text{Ly}\alpha$. The average ratio of the H_2 fluxes (F_{2013}/F_{2011}) is 0.76 ± 0.07 without significant differences between the various routes, i.e., a uniform decrease in all routes (see Fig. G.1 top). The H_2 profile is approximately symmetric at both epochs. If the disk illumination is largely asymmetric, e.g., if the inner warp obscures part of the disk from illumination by the central star, no symmetric emission profile would be observed unless the warp was in front of or behind AA Tau during the two HST COS observing epochs. However, such a special configuration is unlikely. Allowing a tolerance of 45° in phase, the statistical chance is only 6% to find the inner warp in front or behind AA Tau during both obser-

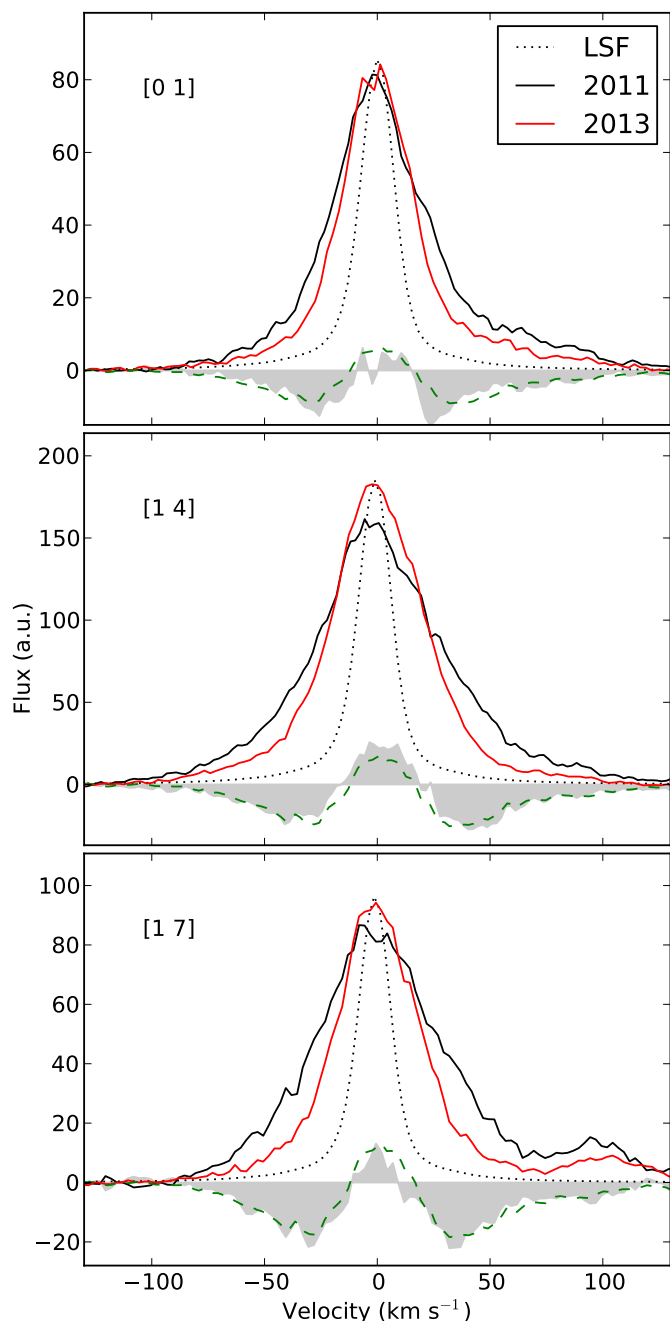


Fig. 6. Flux reduction in the high velocity of the three strongest H_2 progressions. Several lines of the respective progressions have been co-added (to avoid uncertainties in the wavelength calibration, the lines have been shifted to a common zero velocity before co-addition). The shaded area indicates the difference between the two epochs. The mean difference scaled to fit the individual results is shown as the green, dashed curve. An approximate LSF is also shown.

variations. We therefore conclude that the phase of the inner warp does not influence the observed H_2 profile significantly.

The H_2 flux decrease is smaller than the photospheric flux decrease which demonstrates that the majority of the H_2 emission is not subject to the additional absorption, i.e., the upper disk layers are essentially unaffected while the direct sight line toward the star is strongly obscured. This strengthens the interpretation that the extra absorber is located within the disk and not on the outskirts of the system or in the ISM.

Figure 6 shows that the observed flux drops mainly at higher velocities ($|v| \gtrsim 20 \text{ km s}^{-1}$) while the flux close to the line center increases slightly or stays constant. As a rough estimate, we can translate the velocity of 20 km s^{-1} into a radius of about two au using Kepler’s law.

7.2. Disk emission modeling of the H_2 emission

To improve the above rough estimate for the region suffering extra absorption in 2013 compared to 2011, we model the observed H_2 profile with disk emission profiles. We assume the broken power law description for the disk emission of Salyk et al. (2011) and describe the emission as

$$L = a \left(\int_{r_{in}}^{r_{mid}} r^p D(r) dr + \frac{r_{mid}^p}{r_{mid}^q} \int_{r_{mid}}^{r_{out}} r^q D(r) dr \right), \quad (1)$$

where $D(r)$ is the emission per disk annulus. We explored the following parameter space: r_{in} : 0.1 – 0.5 au in steps of 0.1 au, r_{mid} : 0.5 – 5.0 au in steps of 0.2 au. We also experimented with the values for r_{out} , but found little dependence and fixed it to 10 au. The parameters p , q as well as the normalization a were allowed to vary freely. More sophisticated models might describe the true emissivity more accurately. However, we are mainly interested in the change between 2011 (bright state) and 2013 (dim state) so that this description is sufficiently accurate for our purposes. Figure 7 shows the fits and the resulting radial distribution of the disk emission. It shows that the *observed* H_2 emission within about one au is reduced compared to 2011 while the H_2 emission coming from larger radii remained mainly unchanged with approximately the same flux as in 2011.

7.3. Scenarios for the evolution of the H_2 emission

There are two qualitatively different explanations for the reduction of only the high velocity H_2 emission: (I) absorption of the inner disk emission by an outer absorber ($r \gtrsim 1 \text{ au}$) and (II) a reduction of the H_2 excitation in the inner disk. For illustrative purposes, we divide model I into an absorber at about two au (Ia) and an absorber location at larger distances, e.g., 10 au (Ib). Models (Ia) and (Ib) are intended to represent two realizations of an outer absorber that are drawn from a continuum of possible outer absorber locations.

7.3.1. Scenario I: An outer absorber

Scenario Ia: Locating the extra absorber at two au would obscure the high velocity H_2 while leaving the emission from larger radii unchanged. However, such a configuration would also cast a shadow on the parts of the disk behind the absorber as viewed from the stellar surface, i.e., part of the outer disk. This appears unlikely given that the azimuthal extent of the absorber must be $\gtrsim 180^\circ$ to remove about half of the high velocity H_2 emission (red and blue shifted emission are similarly affected). Consequently, a large fraction of the disk at $r > 2 \text{ au}$ would not be illuminated with $Ly\alpha$ photons causing a significant drop in total H_2 flux. Such a severe drop in the H_2 flux would not occur if a similar part of the disk was already in the shadow of the absorber in 2011. As the H_2 profiles are rather symmetric, the absorber should be located at about the opposing location in 2011 (180° phase shift, i.e., mostly behind AA Tau). The orbital period at two au is about 3.2 yrs so that there is sufficient time for the warp to rotate in front of AA Tau between the two FUV observations. However, we know that the dim state lasts more

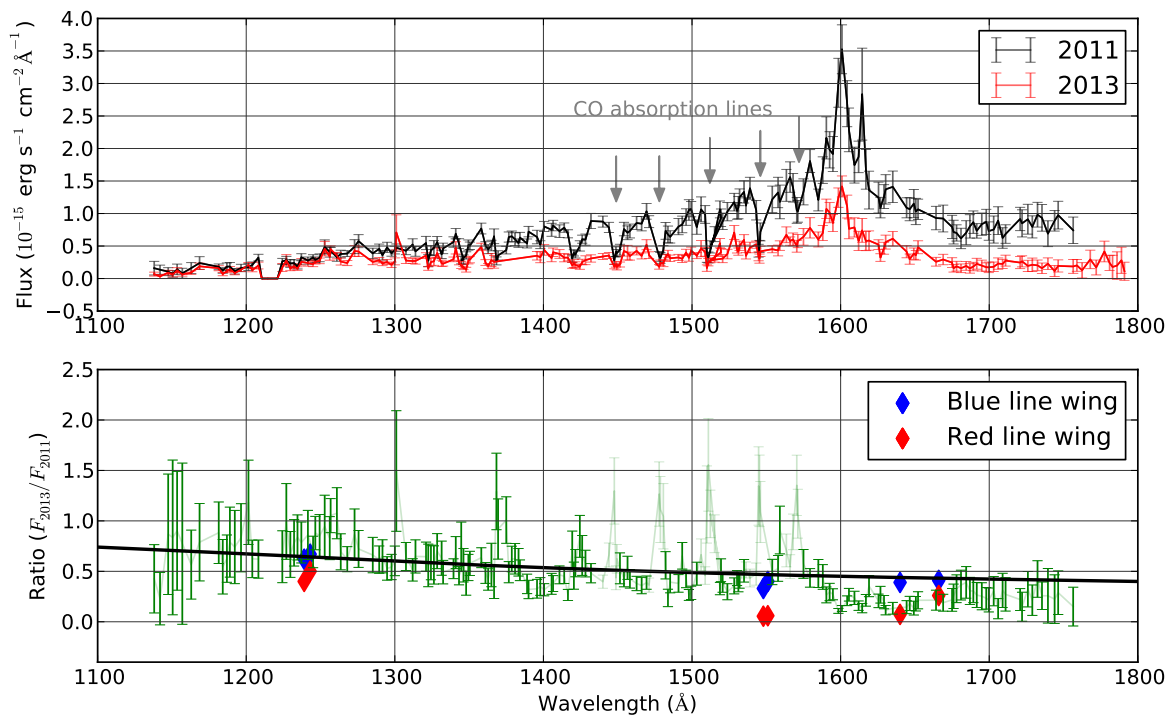


Fig. 8. **Top panel:** FUV continuum of AA Tau. The CO absorption lines are visible. The bump at 1600 Å is also visible. **Bottom panel:** Ratio between both epochs and the ratio between the two transmission curves discussed in the text. Overplotted are the blue and red parts of atomic emission lines.

than four years now, i.e., longer than the orbital period at two au. Therefore, a warp at two au would shadow the outer disk as seen from the star leaving little to no $Ly\alpha$ illumination to pump the H_2 emission. Furthermore, assuming a standard height profile $h(r) = 0.1r^{9/7}$ requires an absorber height of 0.8 au which is four times the value expected ($h \approx 0.1r$) and it is challenging to create a scenario which produces such a massive disturbance of the disk on the orbital time scale.

Scenario Ib: As a variance of the previous scenario, we now locate the absorber at ten au. In that case, only a stripe of the disk would be obscured from view while most regions remain observable from Earth. In addition, the $Ly\alpha$ illuminated disk remains unchanged within ten au where supposedly most of the H_2 emission originates. An azimuthal extent of 20° is sufficient to obscure half of the high velocity H_2 emission. The orbital period at ten au is 35 yrs so that the extra absorber would rotate about 20° within the two years between the two COS observations, i.e., the angular extent needed to obscure part of the inner H_2 emission. Also, the deviation from the $h \approx 0.1r$ relation is reduced compared to the Ia model (height of 1.8 au at ten au from AA Tau) and there is no need for a fast dynamic development. Therefore, we prefer the outer location of the absorber for the cause of the dimming event and the reduction of the high velocity H_2 emission.

7.3.2. Scenario II: Reduced H_2 pumping

Alternatively, a decrease of the high velocity H_2 emission might be caused by reduced H_2 pumping within the inner disk region. An increase of the height of the inner disk wall absorbs the stellar $Ly\alpha$ photons before they can excite H_2 molecules in the inner disk while the outer disk is still illuminated in a flaring disk configuration. However, we consider this scenario unlikely, because

(a) the wall height should be azimuthally symmetric as the high velocity wings are rather symmetric as well, (b) the innermost gas disk where the highest velocity H_2 resides would not be affected contrary to the observations, and (c) the increased inner disk height would not cause the extra absorption towards AA Tau as the viewing angle into the AA Tau system is much larger than the typical angle of the disk height with respect to the midplane ($\tan(i \approx 15^\circ) = 0.27 > 0.1h/r$), i.e., the inner disk wall would completely shadow the disk if it was in the line of sight. Lastly, (d) an increase of the inner disk height would be seen as a flux increase in the K band (or even at shorter wavelengths) which is not observed (the UKIRT data rather suggests less emission from the inner disk). Finally, a scenario where the reduced molecular emission is caused by an inner disk intercepting less $Ly\alpha$ photons due a lower flaring angle appears unlikely, because it is also unrelated to the increased absorption. We therefore prefer an outer absorber as the cause for the dimming.

7.4. FUV continuum emission: Grain growth, scattering or a non-stellar origin?

There is currently no agreement on the origin of the FUV continuum in CTTs. The accretion continuum contributes to the observed flux (especially at longer wavelengths), but a contribution from a yet unidentified emission mechanism might dominate the FUV continuum emission (see discussion in Ingleby et al. 2009; France et al. 2011). Given the two FUV observations that experience different amounts of circumstellar absorption towards the stellar source, we investigate the evolution of the continuum flux to constrain its spatial origin.

Figure 8 shows the evolution of the FUV continuum (extracted from the COS spectra as described in France et al. 2014b). The continuum flux decreases on average by a factor

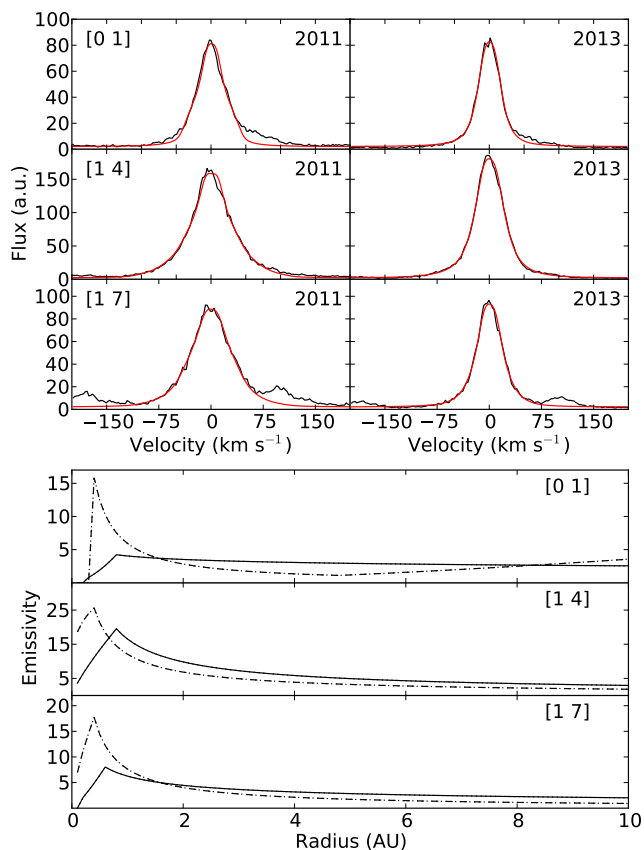


Fig. 7. Modeled H_2 emission lines and emissivity of the disk for the different models. **Top:** Data and model for individual progressions. **Bottom:** Disk emissivity. The 2011 model is shown dash-dotted and the 2013 is the solid curve. Details are given in sect. 7.2.

of about two and is bluer in 2013 than in 2011. The FUV continuum flux decrease is less than the decrease in optical flux between both epochs. Together with the bluer spectral shape, this shows that just adding absorption cannot explain the observed flux evolution. Three qualitatively different possibilities may explain the flux evolution. First, one can replace part of the absorber present in 2011 by an absorber with larger grains (i.e. with $R_V \approx 7$) for the 2013 observation; second, scattering might also contribute to the observed FUV flux; and third, the FUV continuum might not originate close to the stellar surface but within the inner disk region (e.g., at about one au) for which we know from the H_2 flux evolution that the transmission towards this region decreased by a factor of about two. As outlined in App. C, all three possibilities are compatible with available constraints, however, the grain growth scenario does not explain the reduction of the optical brightness modulation by the inner warp so that scattering or a non-stellar origin of the FUV continuum are more likely scenarios. From these two, we favor the non-stellar origin, because one would naively expect that the stellar emission lines and the continuum evolve similarly in the scattering scenario which is not observed. In addition, the flux of the molecular bump at 1600 \AA decreases similarly as the surrounding continuum suggesting that both regions experience the same absorption, i.e., originate in the same region different from the stellar surface. The scattering and non-stellar origin scenarios would also provide a natural explanation for the low molecular column densities obtained from CO absorption against the FUV continuum (McJunkin et al. 2013).

8. Summary and discussion

AA Tau recently experienced a dimming event caused by circumstellar material ($\Delta V \sim 3 \text{ mag}$). We obtained new XMM-Newton X-ray, HST FUV as well as ground-based optical and NIR data of AA Tau during this dim state. The analysis of the FUV H_2 emission lines shows that the absorption is caused by an extra absorber which is most likely located several au from AA Tau, i.e., significantly further out in the system than the inner warp (0.1 au). The decreased NUV to NIR fluxes and the reduced modulation of the optical light curve are best explained by scattering within the circumstellar environment of AA Tau, as already suggested by Bouvier et al. (2013). Since the scattering efficiency strongly decreases towards longer wavelengths, the NIR data most accurately trace the increase in dust extinction between the bright and dim state; we find $\Delta A_V \approx 4.0^{+1.0}_{-0.5}$.

Our X-ray data show that the absorbing gas column density increases by less than a factor of < 1.6 between the dim and the bright state. An increase in absorbing gas column density has just been published by Zhang et al. (2015) from an analysis of mid-IR CO absorption lines observed during the dim state; they find an increase that is higher than our X-ray result assuming the canonical CO to H ratio of 10^{-4} ($N_H^{MIR} > 3.2 \times 10^{22} \text{ cm}^{-2}$ vs $N_H^{X-ray} < 1.5 \times 10^{22} \text{ cm}^{-2}$ and $< 2.0 \times 10^{22} \text{ cm}^{-2}$ for Anders & Grevesse (1989) and Asplund et al. (2009) abundances, resp.). The higher column density is incompatible with the X-ray data (see App. F). We think that the factor of > 1.5 difference is caused by a combination of the following effects. First, the extra absorber might not have the canonical CO-to-H ratio of 10^{-4} although this has been observed for RW Aur (France et al. 2014a). Second, the tension between the parameters (T and b) for FUV and MIR observed CO absorption indicates that the CO absorption model contains additional uncertainty; e.g., T and b were held fixed during all epochs in the Zhang et al. (2015) model which might not be true in this case. Third, the chemical composition of the absorber might differ from the abundance pattern that we used to convert X-ray absorption to hydrogen column density. Appendix F shows that the discrepancy between N_H^{MIR} and N_H^{X-ray} reduces for lower absorber metallicities but remains significant. Fourth, the phase of the inner disk warp might affect the observed CO column density so that the increase in N_H caused by the extra absorber might be lower than the value derived by Zhang et al. (2015).

By comparing X-ray (gas) and optical extinction (dust), we find that the gas-to-dust ratio of the extra absorber is close to the ISM value. This contrasts with previous X-ray data of the AA Tau system that showed a gas-to-dust ratio elevated by about a factor of ten with respect to the ISM for the inner part of the system ($\lesssim 0.1 \text{ au}$) as suggested by previous studies (Schmitt & Robrade 2007; Grosso et al. 2007). Therefore, the new AA Tau X-ray data indicate that the excess gas extinction is restricted to the inner region around the star while the gas-to-dust ratio is within a factor of two to three from the ISM value further out in the system, i.e., gas and dust are well mixed in the part of the disk traced by the sightline through the extra absorber.

The appearance of the extra absorber within a \sim -year time scale calls for an azimuthally asymmetric disturbance of the disk height that rotated into view. Azimuthal asymmetries are often seen in scattered light or thermal dust emission, e.g., LkH α 330 (Isella et al. 2013), but the spatial scales probed by these imaging studies are typically larger than the sizes considered here. The presence of the extra absorber in AA Tau suggests that such asymmetries extend to or at least exist also within about ten au.

In general, X-ray observations indicate enhanced gas-to-dust ratios for CTTs (see, e.g., Tab. 4 in McJunkin et al. 2014, for a recent comparison between dust and X-ray extinction for a number of CTTs). Without the detailed monitoring of the AA Tau system, one could not make the distinction between gas-rich inner region and ISM-like outer region and would divide the total gas column density by the total dust extinction resulting in gas-to-dust that is about twice the ISM-ratio, i.e., the omnipresent gas-rich absorber. However, if the AA Tau result with a gas-rich inner region around the star and a rather ISM-like gas-to-dust ratio further out is representative for CTTs in general, it suggests that the excess gas absorption is caused by material confined to the innermost region (≤ 0.1 au), i.e., accretion funnels or a wind launched close to the star. Such an absorber consisting mostly of gas can significantly reduce the amount of high energy photons impacting the protoplanetary disk without being visible in optical observations. This might have severe consequences for the disk chemistry which strongly depends on the irradiation.

Acknowledgements. It is a pleasure to thank N. Schartel for granting the target of opportunity XMM-Newton observation, S. Wolk for organizing the UKIRT observation, B. Reipurth for providing the UKIRT data, and the CAHA staff for performing the NIR observations in service mode; in particular Aceituno-Castro, Bergond, and the director Galadí-Enríquez for granting the target of opportunity observations. PCS was supported by the DLR under grant 50 OR 1307 and is currently a Research Fellow at ESA/ESTEC. KF acknowledges from a Nancy Grace Roman Fellowship and HMG acknowledges NASA/Chandra Award GO4-15009X issued by the Chandra X-ray Observatory Center for and on behalf of NASA under contract NAS8-03060. We acknowledge LabEx OSUG@2020 that allowed purchasing the imaging system installed at the 1.25-m telescope at CrAO. Based on observations obtained with XMM-Newton, an ESA science mission with instruments and contributions directly funded by ESA Member States and NASA. The paper is also based on observations obtained by the Hubble Space Telescope through Guest Observing Program 12876. Some of the data presented in this paper were obtained from the Multimission Archive at the Space Telescope Science Institute (MAST). STScI is operated by the Association of Universities for Research in Astronomy, Inc., under NASA contract NAS5-26555. Support for MAST for non-HST data is provided by the NASA Office of Space Science via grant NAG5-7584 and by other grants and contracts. We acknowledge with thanks the variable star observations from the AAVSO International Database contributed by observers worldwide and used in this research.

References

Alexander, R., Pascucci, I., Andrews, S., Armitage, P., & Cieza, L. 2014, *Protostars and Planets VI*, 475
 Anders, E. & Grevesse, N. 1989, *Geochim. Cosmochim. Acta*, 53, 197
 Aruda, D. R., Herczeg, G. J., Gregory, S. G., et al. 2013, *ApJS*, 207, 1
 Arnald, K. A. 1996, in *Astronomical Society of the Pacific Conference Series*, Vol. 101, *Astronomical Data Analysis Software and Systems V*, ed. G. H. Jacoby & J. Barnes, 17–+
 Artemenko, S. A., Grankin, K. N., & Petrov, P. P. 2012, *Astronomy Letters*, 38, 783
 Asplund, M., Grevesse, N., Sauval, A. J., & Scott, P. 2009, *ARA&A*, 47, 481
 Bally, J., Feigelson, E., & Reipurth, B. 2003, *ApJ*, 584, 843
 Balucinska-Church, M. & McCammon, D. 1992, *ApJ*, 400, 699
 Basri, G. & Bertout, C. 1989, *ApJ*, 341, 340
 Bouvier, J., Alencar, S. H. P., Bouvier, T., et al. 2007, *A&A*, 463, 1017
 Bouvier, J., Chelli, A., Allain, S., et al. 1999, *A&A*, 349, 619
 Bouvier, J., Grankin, K., Ellerbroek, L. E., Bouy, H., & Barrado, D. 2013, *A&A*, 557, A77
 Bouvier, J., Grankin, K. N., Alencar, S. H. P., et al. 2003, *A&A*, 409, 169
 Cardelli, J. A., Clayton, G. C., & Mathis, J. S. 1989, *ApJ*, 345, 245
 Cox, A. W., Grady, C. A., Hammel, H. B., et al. 2013, *ApJ*, 762, 40
 Danforth, C. W., Keeney, B. A., Stocke, J. T., Shull, J. M., & Yao, Y. 2010, *ApJ*, 720, 976
 Fitzpatrick, E. L. 1999, *Publications of the Astronomical Society of the Pacific*, 111, pp. 63
 France, K., Burgh, E. B., Herczeg, G. J., et al. 2012a, *ApJ*, 744, 22
 France, K., Herczeg, G. J., McJunkin, M., & Penton, S. V. 2014a, *ApJ*, 794, 160
 France, K., Schindhelm, E., Bergin, E. A., Roueff, E., & Abgrall, H. 2014b, *ApJ*, 784, 127

France, K., Schindhelm, E., Burgh, E. B., et al. 2011, *ApJ*, 734, 31
 France, K., Schindhelm, E., Herczeg, G. J., et al. 2012b, *ApJ*, 756, 171
 Grosso, N., Bouvier, J., Montmerle, T., et al. 2007, *A&A*, 475, 607
 Gullbring, E., Hartmann, L., Briceno, C., & Calvet, N. 1998, *ApJ*, 492, 323
 Herczeg, G. J. & Hillenbrand, L. A. 2014, *ApJ*, 786, 97
 Herczeg, G. J., Wood, B. E., Linsky, J. L., Valenti, J. A., & Johns-Krull, C. M. 2004, *ApJ*, 607, 369
 Horne, D., Gibb, E., Rettig, T. W., et al. 2012, *ApJ*, 754, 64
 Hughes, A. M., Wilner, D. J., Qi, C., & Hogerheijde, M. R. 2008, *ApJ*, 678, 1119
 Ingleby, L., Calvet, N., Bergin, E., et al. 2009, *ApJ*, 703, L137
 Isella, A., Pérez, L. M., Carpenter, J. M., et al. 2013, *ApJ*, 775, 30
 Kenyon, S. J., Dobrzycka, D., & Hartmann, L. 1994, *AJ*, 108, 1872
 Lacy, J. H., Knacke, R., Geballe, T. R., & Tokunaga, A. T. 1994, *ApJ*, 428, L69
 Lahuis, F., van Dishoeck, E. F., Boogert, A. C. A., et al. 2006, *ApJ*, 636, L145
 McJunkin, M., France, K., Schneider, P. C., et al. 2013, *ApJ*, 766, 12
 McJunkin, M., France, K., Schneider, P. C., et al. 2014, *ApJ*, 780, 150
 Meyer, M. R., Calvet, N., & Hillenbrand, L. A. 1997, *AJ*, 114, 288
 Predehl, P. & Schmitt, J. H. M. M. 1995, *A&A*, 293, 889
 Rettig, T., Brittain, S., Simon, T., et al. 2006, *ApJ*, 646, 342
 Rieke, G. H. & Lebofsky, M. J. 1985, *ApJ*, 288, 618
 Salyk, C., Pontoppidan, K. M., Blake, G. A., Najita, J. R., & Carr, J. S. 2011, *ApJ*, 731, 130
 Schmitt, J. H. M. M. & Robrade, J. 2007, *A&A*, 462, L41
 Schneider, P. C., Eisloffel, J., Güdel, M., et al. 2013, *A&A*, 550, L1
 Schneider, P. C. & Schmitt, J. H. M. M. 2010, *A&A*, 516, A8
 Skrutskie, M. F., Cutri, R. M., Stiening, R., et al. 2006, *AJ*, 131, 1163
 Smith, R. K., Brickhouse, N. S., Liedahl, D. A., & Raymond, J. C. 2001, *ApJL*, 556, L91
 Strüder, L., Briel, U., Dennerl, K., et al. 2001, *A&A*, 365, L18
 Takeuchi, T. & Artymowicz, P. 2001, *ApJ*, 557, 990
 Testi, L., Birnstiel, T., Ricci, L., et al. 2014, *Protostars and Planets VI*, 339
 Tilling, I., Woitke, P., Meeus, G., et al. 2012, *A&A*, 538, A20
 Turner, M. J. L., Abbey, A., Arnaud, M., et al. 2001, *A&A*, 365, L27
 Valenti, J. A., Basri, G., & Johns, C. M. 1993, *AJ*, 106, 2024
 Weidenschilling, S. J. 1977, *MNRAS*, 180, 57
 Williams, J. P. & Cieza, L. A. 2011, *ARA&A*, 49, 67
 Woitke, P., Kamp, I., & Thi, W.-F. 2009, *A&A*, 501, 383
 Yang, H., Herczeg, G. J., Linsky, J. L., et al. 2012, *ApJ*, 744, 121
 Zhang, K., Crockett, N., Salyk, C., et al. 2015, *ApJ*, 805, 55

Appendix A: Optical magnitudes during the HST observations

The evolution of the optical magnitude between the two HST observations is required to check if particular absorber properties are reasonable, e.g., if they provide a sufficient amount of V band extinction.

For the 2011 HST observation, we use the STIS acquisition images obtained just prior to the COS observations to estimate the optical brightness assuming an effective temperature of 4000 K and $A_V = 0.78$ as found by Bouvier et al. (2013) for the bright state. We find a V-magnitude of about 13.5 which is consistent with a short HST STIS G430L spectrum preceding the COS exposures (the G430L partly overlaps with the V band-pass). This magnitude is typical for the bright state of AA Tau and indicates some absorption by the inner disk warp, because the brightness of the unclipped state has been about 12.5 in the V-band.

For the 2013 HST observation, no preceding optical acquisition images nor optical spectra are available so that we estimate the V-magnitude from contemporary optical data points⁵ (Bouvier et al. 2013). They indicate $V \approx 15$ mag, i.e., about 1.5 magnitudes lower than during the previous COS observations.

Appendix B: Period analysis

Figure B.1 shows phased optical light curves of AA Tau.

⁵ <http://vizier.u-strasbg.fr/local/Vbin/VizieR?-source=35570077>

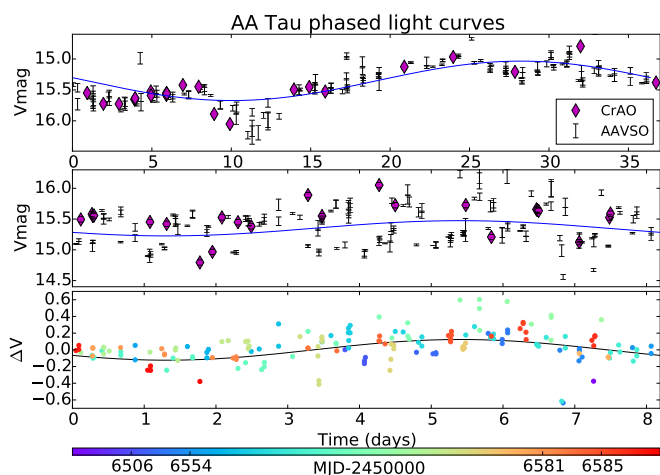


Fig. B.1. Phased optical light curves. The color coding in the bottom panel indicates the observing time as encoded in the colorbar.

Appendix C: FUV continuum evolution

The broad wavelength coverage of the HST COS spectra allows us to determine the wavelength dependent evolution of the FUV continuum flux which, in the simplest scenario, constrains the dust population of the extra absorber. However, additional processes like grain growth, scattering and a non-stellar origin of the FUV continuum hamper direct conclusions and, in fact, none of these three mechanisms can be strictly ruled out.

Appendix C.1: Grain growth

Adding extra extinction cannot cause the continuum to appear bluer in 2013 than in 2011. However, replacing part of the absorber present in 2011 with an absorber that contains on average larger grains causes a bluer continuum. Specifically, replacing ISM-like absorption with $A_V = 0.4$ mag by an absorber with $A_V = 1.9$ and $R_V = 7$ in the Cardelli et al. (1989) description provides a reasonable description of the flux evolution and is compatible with the evolution of the V magnitudes between both epochs (see App. A for the evolution of the V magnitudes between both epochs and Fig. 8 (bottom) for the expected continuum flux evolution).

As we have a better data coverage for the time around the XMM-Newton observation, we checked if adding further 0.6 mag of optical extinction with $R_V = 7$ in the Cardelli et al. (1989) description provides a reasonable description of the flux evolution between the bright state and the dim state around the XMM-Newton observation and found that this, again, requires the brighter NIR fluxes contrary to the observations (see discussion of the grain growth scenario in sect. 5.2). It is impossible to bring the lower NIR fluxes in agreement with the XMM-Newton optical/NUV fluxes by replacing part of an ISM-like absorber during the bright state with an absorber with $R_V > 3.1$ for the 2013 observation. Thus, scattering in the optical is still required to achieve agreement with the lower NIR fluxes when replacing part of the 2011 absorber with an $R_V > 3.1$ one in 2013. Explaining the FUV continuum evolution (moderate flux decrease and blueing) with a modification of the absorber therefore requires scattering in the optical but not in the FUV. In addition, this scenario requires a different explanation for the evolution of the red shifted atomic FUV emission lines which decrease more strongly than the surrounding continuum.

Appendix C.2: Scattering

Scattering can easily explain the blueing of the continuum by postulating that the shortest wavelength already contained scattered photons in 2011 while this did not apply to the same extent to the longer wavelengths. Removing (part of) the direct emission then causes a flux drop as well as a bluer appearance of the continuum. This is compatible with scattering in the optical, but does not explain that the red shifted atomic emission drops more strongly.

Appendix C.3: A non-stellar origin

The analysis of the H₂ emission lines showed that the increased absorption mainly affects the line of sight towards the star while, e.g., emission from the outer disk remained largely unaffected. In particular, the high velocity H₂ emission reduces by about the same fraction as the FUV continuum suggesting that the FUV continuum originates also within the inner few au of the disk. However, the blueing of the continuum remains unexplained in this scenario; potentially scattering also contributes to the continuum even if its origin is not close to the stellar surface or the shape of the non-stellar emission depends on the distance to the star with redder emission predominately emitted at smaller radii. This is compatible with the evolution of the emission bump at 1600 Å seen in both epochs. This bump has been interpreted in terms of a H₂ molecular dissociation quasi-continuum generated by collisions with non-thermal electrons (e.g., Herczeg et al. 2004; Ingleby et al. 2009), i.e., clearly non-stellar. Its flux reduced similarly as the surrounding continuum suggesting that the bump and the majority of the continuum probably experience similar extinction and, thus, probably have a similar spatial origin, too.

To summarize, a non-stellar origin of the FUV continuum is compatible with the observational constraints and scattering might contribute as well while the grain growth scenario appears less likely.

Appendix D: FUV emission lines

The atomic FUV emission lines are usually assumed to be emitted close to the stellar surface and, thus, should experience the same absorption as the photospheric emission. Furthermore, the effect of extinction is more pronounced in the FUV than in the optical. Therefore, we investigate the evolution of the atomic FUV emission lines and concentrate our analysis on the strongest lines (C IV $\lambda\lambda$ 1548, 1551, N V $\lambda\lambda$ 1238, 1242 and He II λ 1640).

Appendix D.1: Details of the data analysis

We removed the H₂ “contamination” from the atomic emission lines using the approach presented by France et al. (2014b), i.e., by fitting the wavelength region under consideration with a number of Gaussians convolved with the instrumental line profile and removing components identified as strong H₂ fluorescence lines. Lastly, we split the lines into a blue and red shifted part, because shock heated gas within the jet can increase the observed blue shifted emission (e.g., C IV in the DG Tau jet, see Schneider et al. 2013). Further, we exclude velocities with $|v| < 50$ km s⁻¹ as the COS wavelength calibration is not accurate to within a few 10 km s⁻¹.

COS does not observe these lines simultaneously so that time variability during the observations can influence the results when comparing data from different wavelength settings. Indeed, there

Table D.2. Extinction values (A_V) for red shifted FUV emission lines. The Cardelli et al. (1989) description of the extinction has been used for the $R_V = 7$ column and “Special” indicates that an ISM-like absorber with $A_V = 0.4$ has been replaced by an $R_V = 7$ absorber with A_V as given in the Table.

Line	Obs. ratio	ISM-like	$R_V = 7.0$	Special
N v	0.34 ± 0.02	0.4	1.3	2.2
C iv	0.04 ± 0.01	1.4	3.6	4.5
He II	0.06 ± 0.01	1.2	3.1	4.1

is minor variability during the 2011 observations with a slight drop of the C iv and N v count-rates over several hours which could change the C iv to N v ratio by about 20% assuming a continuous, linear evolution. In 2013, the rates remain relatively constant (< 10% changes). In the following we neglect these effects, because the variability between the two epochs is much larger.

Appendix D.2: Results

Figure D.1 shows the atomic emission lines and their line fluxes are listed in Tab. D.1 (which also includes the properties of the C II and O III lines). The red and blue shifted emission evolve differently between both epochs with the red shifted part reducing more strongly than the blue shifted one. This might be due to the fact that red shifted emission should be dominated by emission related to the accretion process (accretion funnels or spots) while the blue shifted emission contains a higher fraction of jet/outflow emission which originates above the disk and is, thus, not subject to the extra absorption. For both red and blue shifted emission, the real flux drop might be higher than observed due to scattered photons. In addition, the red line wing might be “contaminated” by broad, slightly blue-shifted emission lines from the outflow/jet. Furthermore, the atomic emission lines in the FUV are time variable so that tight constraints on the properties of the absorber cannot be derived. With these caveats in mind, we describe the evolution of the red and blue shifted emission separately in the following.

Appendix D.2.1: Red shifted emission

The red shifted wing of all atomic emission lines show lower fluxes during the 2013 observation compared to 2011. The fluxes in the red wings of C iv and He II decrease much more strongly than the N v flux (see sum/red wing in Tab. D.1) and more strongly than the FUV continuum. The different evolution of C iv and N v fluxes is unexpected, because both species trace rather similar plasma temperatures ($\log T \sim 5.0$ and 5.3) and are usually well correlated (Yang et al. 2012; Ardila et al. 2013). The N v to C iv ratio is closer to the CTTS correlation (Ardila et al. 2013) in 2013 than in 2011. This suggests that the observed N v flux was unusually low in 2011. Because the N v flux was already low in 2011, its fractional decrease was less than for the other FUV emission lines. We therefore concentrate on C iv and He II in the following.

Tab. D.2 summarizes the absorption required to explain the flux evolution for different descriptions of the FUV extinction assuming no intrinsic variability. It shows that the evolution is compatible with ISM-like absorption based on the evolution of the V magnitude, but incompatible with the evolution of the NIR magnitudes which, unfortunately, have not been obtained simultaneously. The evolution is also compatible with an additional

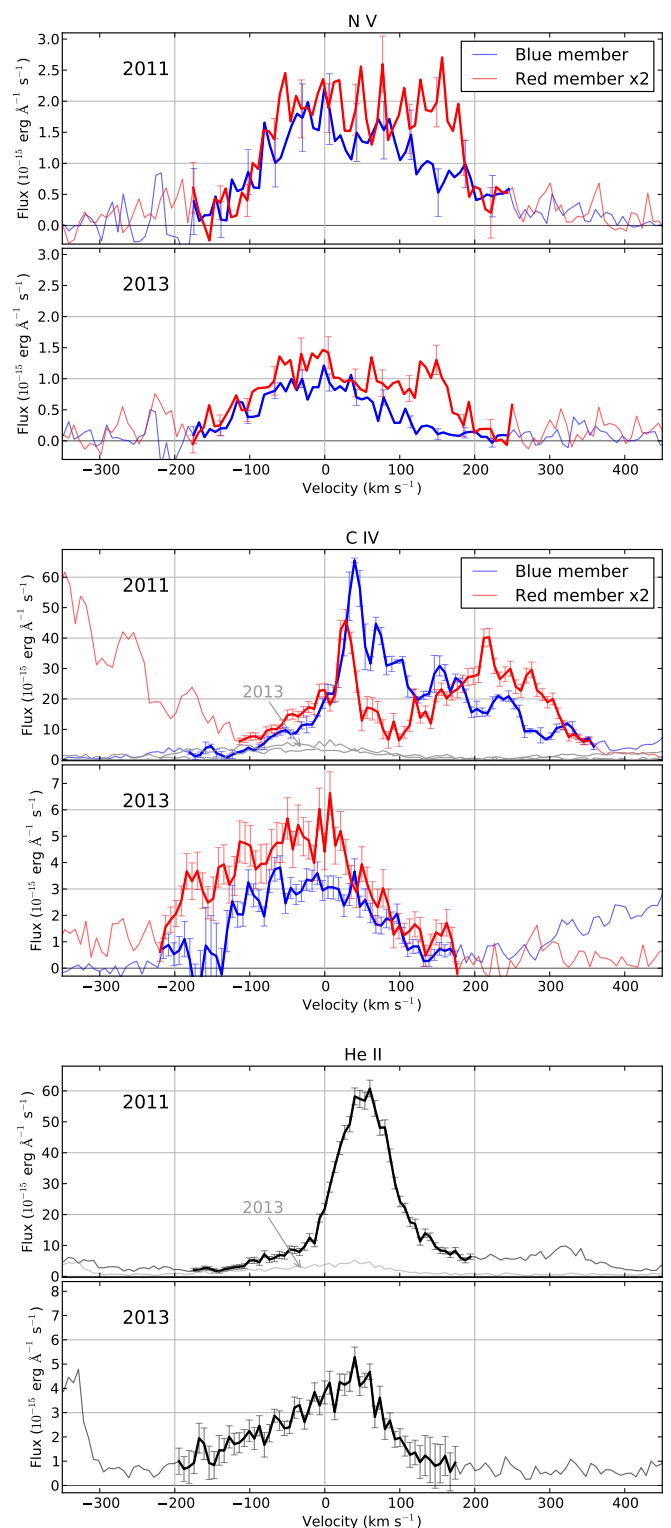


Fig. D.1. Comparison of the blue and red members of the N v and C iv doublets as well as the evolution of the He II line. The red members have been scaled by a factor of two to easily see the optical depth effects. The relevant parts of the lines are drawn with thick lines and errors.

$R_V = 7$ absorber. In addition, it is possible to replace part of an ISM-like absorber in 2011 by an $R_V = 7$ absorber assuming scattering contributes to the observed optical but not to the FUV fluxes since this is still compatible with the range of observed NIR magnitudes. Given potential intrinsic time variability, the

Table D.1. Line fluxes for selected atomic lines and continuum

Line-ID	Rest wavelength (Å)	Velocity range (km s ⁻¹)	Flux 2011 (10 ⁻¹⁵ erg s ⁻¹ cm ⁻²)	Flux 2013 (10 ⁻¹⁵ erg s ⁻¹ cm ⁻²)	Ratio
N v	1238.8	-130 ... +240	1.71 ± 0.05	0.77 ± 0.02	0.45 ± 0.02
	1242.8	-130 ... +240	1.16 ± 0.04	0.65 ± 0.02	0.56 ± 0.03
	sum	blue wing	0.79 ± 0.04	0.58 ± 0.02	0.73 ± 0.05
		red wing	1.78 ± 0.05	0.6 ± 0.02	0.34 ± 0.02
C II	1335.7	total ^a	2.46 ± 0.05	1.30 ± 0.03	0.53 ± 0.02
C IV	1548.2	-300 ... 150	32.53 ± 0.38	3.56 ± 0.16	0.110 ± 0.005
		total ^b	50.09 ± 0.45	3.56 ± 0.16	0.071 ± 0.003
	1550.8	-80 ... 400	22.50 ± 0.34	2.36 ± 0.09	0.105 ± 0.004
		total ^c	22.50 ± 0.34	3.74 ± 0.10	0.166 ± 0.005
	sum	blue wing	7.1 ± 0.2	3.5 ± 0.2	0.49 ± 0.03
		red wing	57.3 ± 0.5	2.1 ± 0.1	0.04 ± 0.01
O III]	1666.2	total ^d	2.76 ± 0.20	0.85 ± 0.08	0.30 ± 0.04
		-300 ... +150	1.75 ± 0.16	0.85 ± 0.08	0.49 ± 0.06
		blue wing	0.72 ± 0.10	0.43 ± 0.05	0.59 ± 0.11
		red wing	0.97 ± 0.10	0.24 ± 0.05	0.24 ± 0.06
He II	1640.4	-240 ... 200	32.11 ± 0.41	3.00 ± 0.15	0.093 ± 0.005
		blue wing	2.09 ± 0.16	1.05 ± 0.09	0.50 ± 0.06
		red wing	23.94 ± 0.34	1.32 ± 0.10	0.06 ± 0.01
Continuum			Average Flux 2011 ^e	Average Flux 2013	Ratio
Wavelength range			(10 ⁻¹⁵ erg s ⁻¹ cm ⁻² Å)	(10 ⁻¹⁵ erg s ⁻¹ cm ⁻² Å)	
λ < 1300 Å			0.26 ± 0.01 (4.0)	0.19 ± 0.01 (3.0)	0.73 ± 0.05
1300 < λ < 1600 Å			0.79 ± 0.01 (24.4)	0.39 ± 0.01 (10.4)	0.49 ± 0.01
λ > 1600 Å			0.90 ± 0.01 (42.1)	0.37 ± 0.01 (16.5)	0.41 ± 0.01

^a 0 ... 200 for 2013, 10 ... 250 for 2013

^b -300 ... + 400 for 2011, -300 ... + 150 for 2013

^c -80 ... + 400 for 2011, -300 ... + 350 for 2013

^d -300 ... 540 for 2011, -300 ... 150 for 2013

^e Numbers in brackets give integrated fluxes in units of 10⁻¹⁴ erg s⁻¹ cm⁻²

FUV emission lines are compatible with the different absorber properties discussed above. Furthermore, they are even compatible with higher A_V values for an ISM-like absorber assuming that scattering operates also on the atomic FUV emission lines or emission in the red shifted wing of a blue shifted emission component contributes to the red shifted velocity range.

Appendix D.3: Blue shifted atomic emission

The evolution of the blue line wings of the atomic emission lines is visualized in Fig. 8. The blue wings decrease similarly as the surrounding FUV continuum. This suggests that both components are similarly affected by the extra absorber, i.e., less strongly than the red shifted emission originating close to the stellar surface.

Interpreting the continuum emission in terms of a non-stellar origin easily reconciles the evolution of the blue shifted atomic emission lines as they probably originate partly in the outflow/jet, i.e., above the disk. In particular, the C IV emission in 2013 appears slightly blue shifted and rather Gaussian shaped as expected for an outflow/jet origin. Whether the observed atomic emission traces knots within the jet as in DG Tau (Schneider et al. 2013) or a hot stellar wind remains undecided. The similar evolution of blue shifted atomic emission lines and continuum favors a similar spatial origin. Knots within the jet further away from the source would not be affected by the extra absorber, so that the an origin close to the disk is likely which favors a stellar wind as the origin of the blue shifted emission lines.

Appendix E: CO emission

Fluorescent CO emission traces the coolest FUV-emitting plasma observed in our COS spectra. With a typical temperature of a few hundred K it is significantly colder than the observed H₂ emission (about 2 – 3 × 10³ K, France et al. 2011). The flux of the strong CO emission lines is constant indicating that the CO emitting region is not significantly affected by the extra absorber and that the pumping radiation field did not change significantly between the two FUV observations.

In principle, we could also apply the disk emission modeling to the CO emission to constrain the spatial origin of the emission. Unfortunately, this is only possible with some accuracy for the CO data from 2013 but not for 2011. Figure E.1 shows that the CO disk emissivity peaks at slightly larger radii than the H₂ disk emissivity (CO: 1.2 au, H₂: 0.6-0.8 au), but appears in general rather similar to the H₂ models for 2013. Therefore, the CO emission comes from similar regions within the disk as the H₂ in 2013. Since the total flux did not change significantly, a similar spatial origin in 2011 is likely. This again indicates that only the disk emission within one to two au is affected by the extra absorber.

Appendix F: CO absorption

Figure E.2 shows the evolution of the CO absorption seen in COS. To compare the CO absorption between both epochs, we fit the continuum data (see sect. C) around the CO absorption

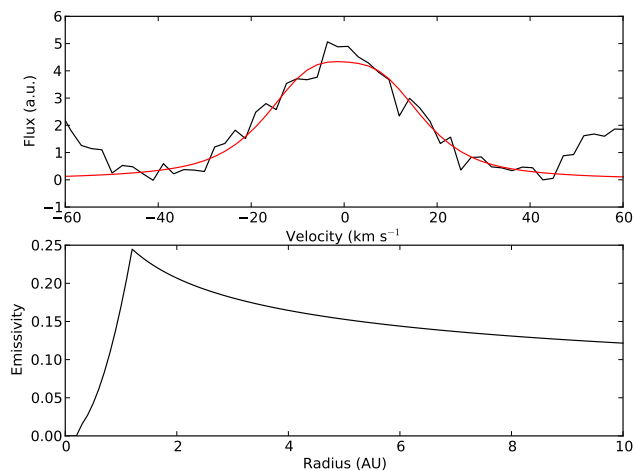


Fig. E.1. Top: Fit to the 2013 CO emission. Bottom: Emissivity of the disk.

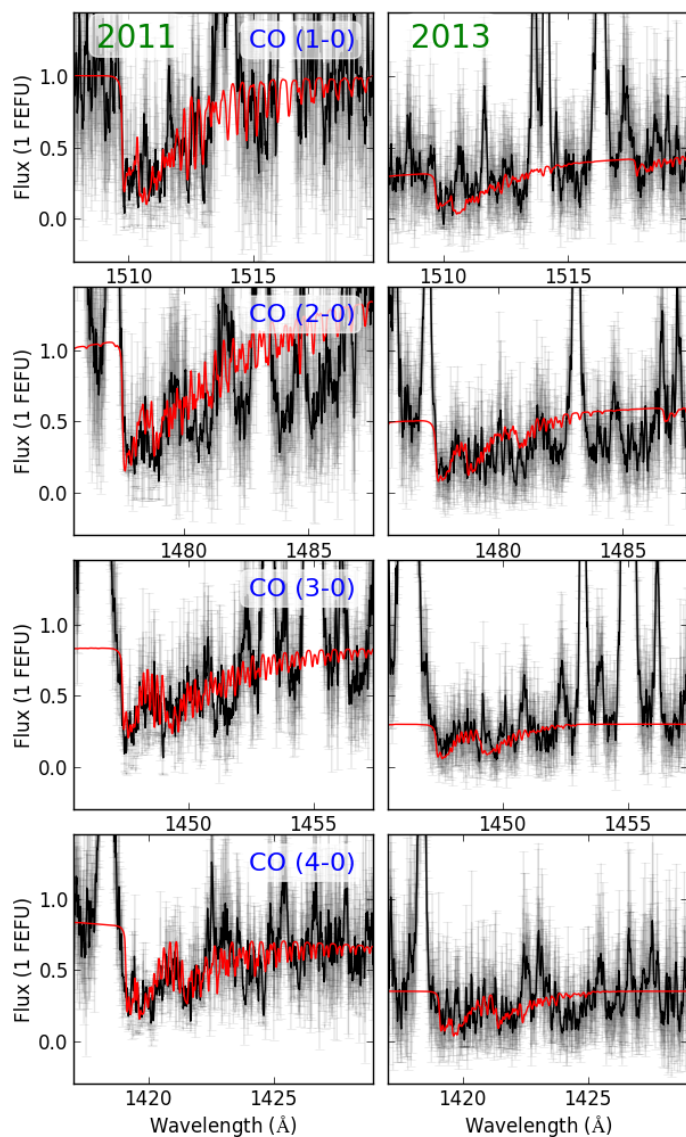


Fig. E.2. CO absorption bands with fits.

bands with a first order polynomial excluding the data falling into the wavelengths ranges of the 1-0 to 4-0 absorption bands. Using this continuum, we calculate an “equivalent width” (EW) of the CO absorption by summing the wavelengths regions unaffected by H₂ emission and find that the EW decreases by about 10–21 % between both epochs (1 σ confidence range). Including the uncertainty in the continuum level which we assume to be about 10 and 15 % for the 2011 and 2013 data, the EW ratio between both epochs is 1.16 ± 0.40 . Thus, the CO absorption column densities are similar unless the Doppler broadening parameter b differs significantly between both epochs. Unfortunately, b is not well constrained due to the large instrumental line width (17 km s^{-1}) compared to the b value which is usually around 1 km s^{-1} (McJunkin et al. 2013). Nevertheless, we attempted to fit the CO absorption using the methods of McJunkin et al. (2013) and find a best fit CO column density of $2.5 \times 10^{18} \text{ cm}^{-2}$, a temperature of 100 K and a Doppler b value of 0.5 km s^{-1} for the 2013 data. This column density is about an order of magnitude higher than that derived by France et al. (2012a) for the 2011 observation, which is mainly caused by the lower b value (0.5 vs 1.2 km s^{-1}), but also by the much cooler temperature (100 vs. 500 K). However, the errors on the CO column densities are about 1 dex. In summary, we find no significant increase of the CO absorption column density.

While working on the revised version of this paper, Zhang et al. (2015) published CO mid-IR data of AA Tau during the dim state. They find $N_{12\text{CO}} = 3.2 \times 10^{18} \text{ cm}^{-2}$, which is close to our best fit value from the FUV CO absorption. However, their temperature and broadening values ($T \approx 494 \text{ K}$ and 2.2 km s^{-1} , resp.) differ significantly from our absorption model. Adopting their higher broadening value would strongly decrease the column density required to explain the FUV CO absorption. We thus conclude that both measurements might not trace the same absorber. Given that scattering might contribute to the observed FUV emission, one possibility is that the FUV absorption traces CO located at higher disk altitudes than the MIR CO absorption which is unaffected by scattering.

Using the canonical CO to H ratio of 10^{-4} , Zhang et al. (2015) estimate $N_{\text{H}} > 3.2 \times 10^{22} \text{ cm}^{-2}$ for the extra absorber, which is of the same order of magnitude as our column density derived from the X-ray data. However, their lower limit is incompatible with the X-ray data. Using the minimum column density absorbed in 2003 ($N_{\text{H}} = 0.9 \times 10^{22} \text{ cm}^{-2}$) plus their minimum column density ($N_{\text{H}} = 3.2 \times 10^{22} \text{ cm}^{-2}$) for the extra absorber results in $N_{\text{H}} > 4.1 \times 10^{22} \text{ cm}^{-2}$, but models with $N_{\text{H}} = 4.1 \times 10^{22} \text{ cm}^{-2}$ do not provide an acceptable fit to the X-ray data. They result in $\chi^2 = 86$ (51 d.o.f.) using the Anders & Grevesse (1989) abundances and in $\chi^2 = 78$ using the Asplund et al. (2009) abundances, respectively. The best fitting model has $\chi^2 = 33/34.5$ (Anders & Grevesse (1989), Asplund et al. (2009) abundances, resp.). The 90 % confidence range upper limit on the absorbing column density from the X-ray data is $2.3 \times 10^{22} \text{ cm}^{-2}$ (Anders & Grevesse 1989) and $3.3 \times 10^{22} \text{ cm}^{-2}$ (Asplund et al. 2009).

Appendix G: Additional H₂ information

Table G.1 lists the properties of the detected H₂ progressions and Fig. G.1 shows the evolution of the fluxes and width of the H₂ lines.

Table G.1. Properties of the molecular hydrogen progressions during the two epochs.

[v' , J']	FWHM (km s ⁻¹)		Flux (10 ⁻¹⁴ erg cm ⁻² s ⁻¹)	
	2011	2013	2011	2013
[0, 1]	44.4 ± 13.9	30.7 ± 1.7	31.0 ± 4.8	24.7 ± 0.8
[1, 4]	64.9 ± 6.6	43.1 ± 4.1	55.6 ± 9.1	49.5 ± 5.3
[1, 7]	61.8 ± 3.8	36.7 ± 2.5	29.0 ± 1.8	22.1 ± 1.3
[2, 12]	39.0 ± 4.2	35.9 ± 6.2	9.6 ± 0.5	6.0 ± 0.7
[0, 3]	48.2 ± 7.4	36.8 ± 7.1	1.1 ± 0.5	1.8 ± 0.1
[0, 2]	47.9 ± 11.3	42.5 ± 9.7	30.9 ± 5.8	18.9 ± 4.0
[3, 0] ¹	70.8 ± 40.2	57.5 ± 48.2	5.8 ± 1.6	3.2 ± 1.0
[4, 4] ¹	60.7 ± 24.7	30.2 ± 9.2	7.3 ± 4.8	6.8 ± 1.5
[4, 13] ¹	78.1 ± N/A	36.7 ± N/A	17.6 ± N/A	12.9 ± N/A

¹ Low-quality 2011 fits, comparison probably not meaningful

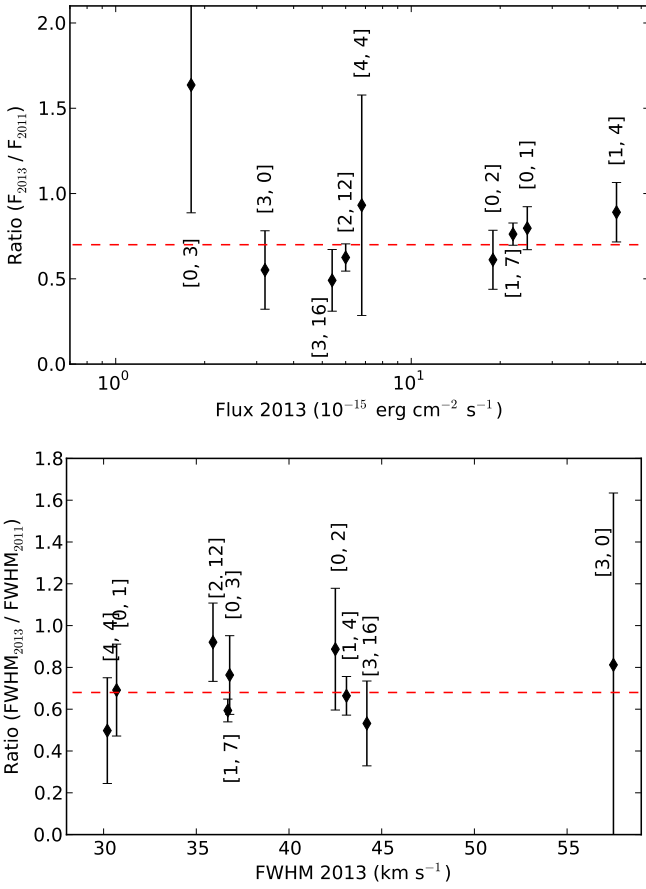


Fig. G.1. Evolution of the H₂ flux and FWHM for different progressions.